

MIT Open Access Articles

Bubble growth and departure modes on wettable/non-wettable porous foams in alkaline water splitting

The MIT Faculty has made this article openly available. **Please share** how this access benefits you. Your story matters.

Citation: Iwata, Ryuichi, Zhang, Lenan, Wilke, Kyle L, Gong, Shuai, He, Mingfu et al. 2021. "Bubble growth and departure modes on wettable/non-wettable porous foams in alkaline water splitting." *Joule*, 5 (4).

Published Version: 10.1016/J.JOULE.2021.02.015

Publisher: Elsevier BV

Permanent Link: <https://hdl.handle.net/1721.1/142051>

Version: Author's final manuscript: final author's manuscript post peer review, without publisher's formatting or copy editing

Terms of use: <http://creativecommons.org/licenses/by-nc-nd/4.0/>



1 Bubble growth and departure modes on wettable/non-wettable porous
2 foams in alkaline water splitting

3 Ryuichi Iwata^{1,4}, Lenan Zhang^{1,4}, Kyle L. Wilke¹, Shuai Gong^{1,2}, Mingfu He¹, Betar M. Gallant¹
4 and Evelyn N. Wang^{1,3,*}

5 ¹Department of Mechanical Engineering, Massachusetts Institute of Technology, 77
6 Massachusetts Avenue, Cambridge, Massachusetts 02139, United States

7 ²School of Mechanical Engineering, Shanghai Jiao Tong University, 800 Dongchuan Road,
8 Shanghai 200240, China

9 ³Lead Contact

10 ⁴These authors contributed equally to this work.

11 *Correspondence: enwang@mit.edu (E. N. W.)

12 KEYWORDS: Gas-evolving reaction, porous foam electrode, alkaline electrolysis, wettability,
13 overpotential

14

15 **SUMMARY**

16 Bubble growth and departure are ubiquitous phenomena in gas-evolving reactions, which govern
17 the overall energy and mass transport. However, an in-depth understanding of the relationship
18 between bubble dynamics and the electrochemical processes, in particular, the wettability effect
19 on a gas-evolving porous electrode remains elusive. Here, we report the bubble dynamics and
20 overpotential observed during alkaline water splitting on a polytetrafluoroethylene (PTFE)
21 deposited nickel porous electrode. With only a slight decrease in hydrophilicity (where the bubble

1 receding contact angle increased from 5° to 12°), the transport overpotential increased two times
2 for a broad range of current densities. We show that the porous electrode transitioned from a liquid-
3 filled state to a gas-filled state when varying the wettability, which changed the bubble departure
4 sizes and bubble coverage. As a result, there were substantial changes of the transport
5 overpotential. Our work elucidates the fundamental relationship between wettability and water
6 splitting characteristics, which provides a practical scenario to structure the electrode for gas-
7 evolving reactions.

8

9 **Context & Scale**

10 Electrochemical gas-evolving reactions play a crucial role in many industrial energy conversion
11 and storage processes. The continuous gas production leads to the evolution of bubbles at the
12 reaction sites, which further results in energy loss due to the increase of transport resistance. To
13 enable high-performance electrochemical systems, bubble dynamics during gas-evolving reactions
14 have attracted particular interest recently. Yet, the fundamental relationship among gas-evolving
15 electrode wettability, bubble dynamics and overpotential has not been well-understood. In this
16 work, we investigate the bubble dynamics and the resulting overpotential in alkaline water splitting
17 by engineering the wettability of a porous electrode. We show that a slight decrease in wettability
18 could result in a drastic transition of bubble dynamics and a significant increase of the transport
19 overpotential. We explained this transition behavior by comparing the wettability dependent
20 bubble departure size and the characteristic pore size of the electrode. The insights gained from
21 this study not only shed light on the fundamentals among electrode wettability, bubble dynamics
22 and overpotential, but also provide design guidelines for porous electrodes to enable high-
23 performance gas-evolving reactions.

1 INTRODUCTION

2 Gas-evolving reactions are ubiquitous in many electrochemical systems including water splitting,
3 chlor-alkali electrolysis, and direct methanol fuel cells.¹⁻⁸ Bubble formation due to the limited
4 solubility of reactants in the electrolyte reduces the effective reaction area, increases the ohmic
5 resistance and creates undesired ion concentration, which becomes one of the most dominant
6 mechanisms for overpotential on gas-evolving electrodes.⁹⁻¹³

7 To reduce energy losses and thus improve production efficiency, investigation on gas bubble
8 dynamics in electrochemical systems remains an active topic despite its long history.^{1,2,5,14-19} In
9 particular, recent studies showed that the change of wettability of electrodes, enabled by either
10 depositing a hydrophobic material²⁰ or fabricating micro/nanostructures on a flat substrate,²¹⁻²³
11 plays an important role in bubble dynamics such as heterogeneous nucleation,^{24,25} bubble
12 growth,^{26,27} and bubble departure size,^{20,23} leading to different water splitting characteristics.²³ In
13 a water splitting system, the overpotential is known as the additional voltage required on top of
14 the thermodynamic voltage (1.23 V) to trigger water splitting.³ During an oxygen evolution
15 reaction process, the total overpotential η_{total} from the reference electrode (RE) to working
16 electrode (WE) consists of the activation overpotential for oxygen evolution reaction (OER) η_{act} ,
17 cell ohmic overpotential $\eta_{ohm,cell}$, bubble ohmic overpotential $\eta_{ohm,bub}$, concentration overpotential
18 η_{con} and bubble overpotential η_{bub} ,

$$19 \eta_{total} = \eta_{act} + \eta_{ohm,cell} + \eta_{ohm,bub} + \eta_{con} + \eta_{bub}. \quad (\text{Equation 1})$$

20 Note that $\eta_{ohm,cell}$ represents the intrinsic cell ohmic drop due to the circuit and solution resistance,
21 whereas $\eta_{ohm,bub}$ is induced by the bubble layer on the electrode surface.^{28,29} η_{con} is dominated by
22 the bubble growth-and-departure induced micro-convection,^{30,31} and η_{bub} results from the decrease

1 of effective reaction area due to bubble coverage.^{10,32,33} Therefore, $\eta_{ohm,bub} + \eta_{con} + \eta_{bub}$ is defined
2 as the transport overpotential (η_{trans}), which is closely related to the bubble dynamics on both the
3 anode and cathode and becomes significant for high current density conditions.^{3,9,32} At the
4 fundamental level, although engineered flat substrates have been used to study bubble dynamics,
5 the wettability effect on a porous electrode, which is more commonly used in practice due to its
6 high specific area and mass transport performance,³⁴⁻⁴⁰ remains not well-understood. Recently,
7 Kempler *et al.* observed that the bubble dynamics on a micropillar structured electrode vary with
8 the micropillar pitch and diameter, indicating that the wettability of microstructured electrode
9 could play a significant role to bubble behavior.²⁹ Kang *et al.* also reported the wettability effect
10 on overpotential using different porous transport layers.⁴¹ However, quantitatively relating the
11 bubble wetting state to bubble dynamics during gas-evolving reactions remains elusive. From a
12 practical perspective, optimizing the electrode porous structure with known material wettability or
13 engineering the wettability based on a fixed porous structure is important for the design of gas-
14 related electrochemical systems. For example, since the kinetics of a given catalyst can be
15 optimized by engineering its wettability,^{42,43} it is necessary to fill the knowledge gap and determine
16 how to design the architecture of the porous electrode based on the wettability of the catalyst. This
17 understanding would, therefore, helps bridge fundamental materials insights with practical
18 electrolyzer design.

19 In this work, we studied the relationship among the porous electrode wettability, bubble dynamics
20 and the resulting transport overpotential using alkaline water splitting as an example. We measured
21 the transport overpotential on a nickel foam, where its wettability was well-controlled through a
22 nickel/polytetrafluoroethylene (PTFE) co-deposition process.⁴⁴ By changing the wettability of the
23 electrode with different PTFE coverage Θ_{PTFE} (the ratio of projected PTFE surface area to the total

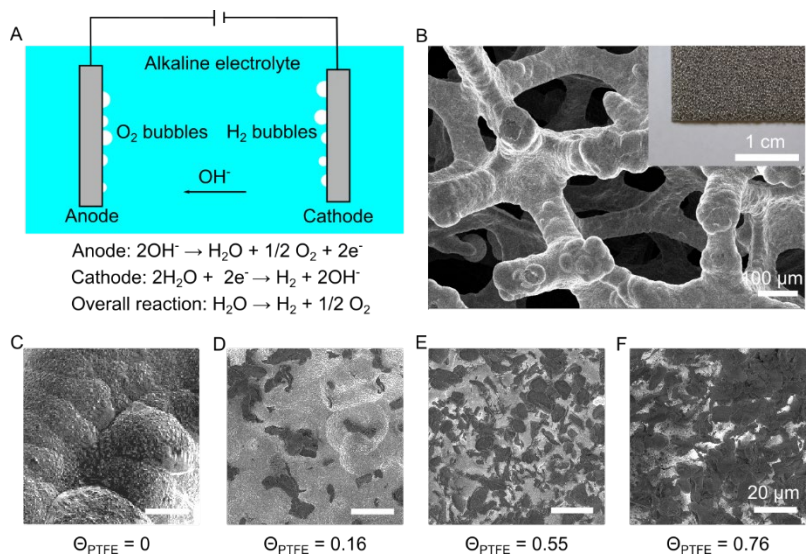
1 projected area), we show a significant change of the transport overpotential on the same porous
2 structure, which is comparable to or even greater than the activation overpotential for state-of-the-
3 art catalysts at a high current density.^{45,46} To understand this phenomenon, we studied the wetting
4 state of the nickel foam with different PTFE coverage ($\Theta_{PTFE} = 0, 0.16, 0.55$ and 0.76). The wetting
5 state transitioned from a superhydrophilic to superhydrophobic state due to the porous structure
6 and PTFE coating, which can be well-described by modified Cassie-Baxter and Wenzel equations.
7 The significant change of wetting state led to different bubble growth and departure modes. As a
8 result of the increase in the bubble departure diameter, bubble layer thickness and bubble coverage
9 increased which contributed to the significant increase in transport overpotential. Based on the
10 insights gained from bubble dynamics, we extracted an important design parameter relating the
11 wettability effect to electrode structure, *i.e.*, the ratio of bubble departure diameter and pore
12 diameter. When the electrode operates in a mass transport loss dominated regime, this ratio should
13 be less than one to ensure that the reaction area enhancement using a porous structure can be
14 maintained.

15

16 **RESULTS AND DISCUSSIONS**

17 We studied alkaline water splitting driven by an external electrical potential where oxygen bubbles
18 formed on the anode and hydrogen bubbles formed on the cathode (Figure 1A). Nickel foam with
19 $\approx 95\%$ porosity, $\approx 400 \mu\text{m}$ pore diameter and $\approx 1.6 \text{ cm}$ thickness was used as the WE for OER.
20 The high porosity and small pore size were confirmed by a scanning electron microscope (SEM,
21 Zeiss Merlin High-resolution SEM) as shown in Figure 1B. In addition, many microscale
22 hierarchical bumpy structures were observed (Figure 1C) on the nickel porous structure, which

1 increased the effective reacting area and the wettability due to the bubbles residing in the Wenzel
 2 state.⁴⁷ PTFE powders (Goodfellow, $\approx 6\text{-}9\ \mu\text{m}$ diameter) were deposited onto the nickel porous
 3 structure (Figure 1D-F). Four nickel foams with various PTFE coverage (0 , 0.16 ± 0.02 , $0.55 \pm$
 4 0.03 and 0.76 ± 0.02 , respectively) were prepared by changing the concentration of deposition
 5 solution and deposition time (see Experimental Procedures and Supplemental Information for
 6 details of sample preparation and PTFE coverage characterization), where the coverage was
 7 characterized by SEM (Figures 1C-F). The reason that the nickel foam coated with PTFE powders
 8 was selected as our material system is to achieve a large range of wettability. This large tunability
 9 of wetting state, from superhydrophilic to superhydrophobic which will be confirmed later, ensures
 10 that our analysis can span most of the design conditions for the practical systems.



11
 12 **Figure 1. Nickel porous electrodes for water splitting.**

13 (A) Schematic of the alkaline water splitting involving an oxygen evolution reaction (OER) and a
 14 hydrogen evolution reaction (HER).

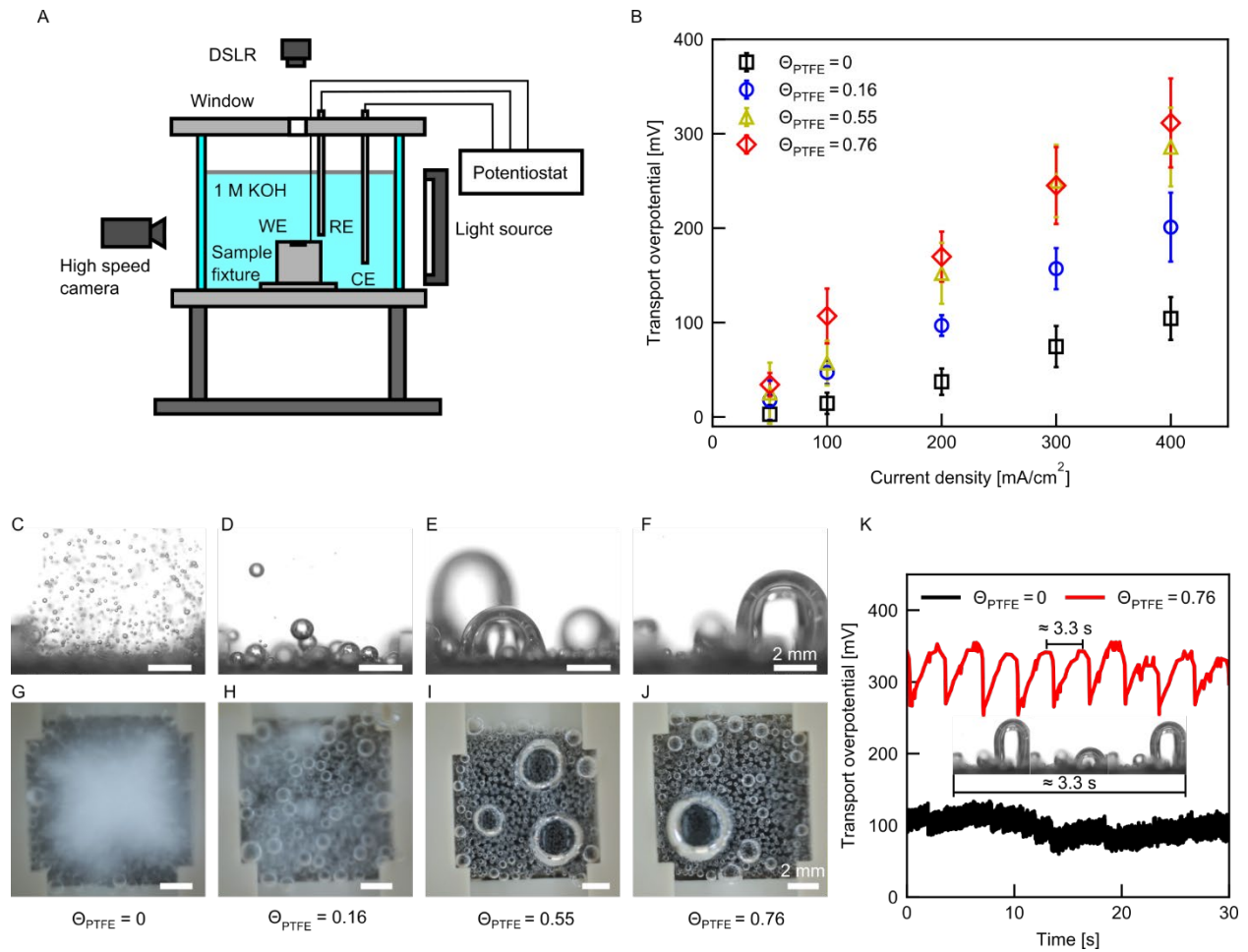
1 (B) SEM image of bare nickel foam (porosity: 95%, number of pores: 20 /cm, thickness: 1.6 mm).
2 The inset image shows the bulk material of the nickel foam.

3 (C), (D), (E), (F) SEM images of nickel foams after electrodeposition. PTFE concentration in the
4 deposition solution are 0 g/L, 10 g/L, 30 g/L and 45 g/L, respectively with deposition time, 10
5 min, 10 min, 60 min and 45 min, respectively. PTFE coverage was determined based on the SEM
6 images as 0, 0.16 ± 0.02 , 0.55 ± 0.03 and 0.76 ± 0.02 , respectively. Scale bars are all 20 μm .

7
8 Figure 2A shows a schematic of a standard three-electrode experimental setup used for our testing.
9 The nickel foam (10 mm \times 10 mm) was horizontally positioned on a sample fixture and used as the
10 WE. The graphite electrode and the Ag/AgCl electrode were used as a counter electrode (CE) and
11 a RE, respectively. The OER polarization curves were obtained by linear sweep voltammetry at a
12 scan rate 1 mV/s. The measured potential was calibrated to the reversible hydrogen electrode
13 (RHE) by the equation: $E_{RHE} = E_{Ag/AgCl} + 0.197 \text{ V} + 0.059 \text{ pH}$ where E_{RHE} is the potential against
14 RHE and $E_{Ag/AgCl}$ is the potential against the Ag/AgCl electrode. In addition, OER experiments
15 under constant current density conditions (50, 100, 200, 300, 400 mA/cm²) were conducted for
16 bubble visualization and transport overpotential analysis on samples with different PTFE coverage
17 (0, 0.16, 0.55, and 0.76, respectively). To visualize the oxygen bubble dynamics, a high-speed
18 camera (Phantom v7.1, Vision Research Inc.) was placed on the side and a digital single-lens reflex
19 (DSLR) camera (EOS rebel T3, Canon) was mounted on top, and were illuminated by a diffuse
20 light source (Fiber-Lite MODEL3100, Dolan-Jenner Industries, Inc.). The transport overpotential
21 η_{trans} was obtained by subtracting the contribution of the cell ohmic overpotential $\eta_{ohm,cell}$ and
22 activation overpotential η_{act} , which were determined by electrochemical impedance spectroscopy

1 (EIS) and Tafel fitting without the presence of bubbles, respectively (see Figures S1 and S2 in
2 Supplemental Information). The OER process was performed in 1 M KOH solution. Figure 2B
3 shows the transport overpotential as a function of current density with four different PTFE
4 coverages. To investigate the role of wettability and bubble dynamics on the transport
5 overpotential, the overpotential owing to the decrease of effective reaction area with PTFE
6 coverage was carefully calibrated and excluded from the transport overpotential in Figure 2B (see
7 Figure S1 in Supplemental Information). Significant differences in transport overpotential on the
8 WE were obtained by changing PTFE coverage for the wide range of current densities.
9 Specifically, the lowest transport overpotential was observed on the WE without PTFE, whereas
10 it increased over three times when the PTFE coverage increased from 0 to 0.76. As an example,
11 the transport overpotential increased from 104 mV to 311 mV at a current density of 400 mA/cm²
12 when increasing the PTFE coverage from 0 to 0.76. Note that the difference in transport
13 overpotential for nonwetable and wettable electrodes in this experiment was comparable to or
14 even greater than the activation overpotential for state-of-the-art catalysts at a high current
15 density.^{45,46} In other words, designing the pore structures and the wettability could be equally
16 important as designing the catalyst to a practical electrolyzer. Meanwhile, a drastic change in the
17 bubble behaviors was observed with the increase of PTFE coverage (Figures 2C-J), indicating a
18 strong dependence between bubble dynamics and transport overpotential. When no PTFE was
19 deposited on the WE ($\theta_{PTFE} = 0$), many oxygen bubbles smaller than the pore diameter of the WE
20 ($\sim 200 \mu\text{m} - 700 \mu\text{m}$) were generated (Figures 2C, 2G and see Supplemental Video S1 for bubble
21 dynamics visualization). For PTFE coverage $\theta_{PTFE} = 0.16$, the oxygen bubbles became much
22 larger than those in the $\theta_{PTFE} = 0$ condition, which are comparable to the pore diameter (Figures
23 2D, 2H and see Supplemental Video S2 for bubble dynamics visualization). A significant transition

1 in bubble behavior was observed when the PTFE coverage increased to $\Theta_{PTFE} = 0.55$, where
2 several very large bubbles (> 2 mm diameter) were observed, while the surrounding bubbles were
3 generally small (< 1 mm diameter, Figures 2E and 2I). Bubbles residing on the WE became the
4 hemispherical shape (Figures 2E and 2I). When the PTFE coverage increased to 0.76, the bubbles
5 behaved similar to the condition of PTFE coverage $\Theta_{PTFE} = 0.55$, with a slight increase of bubble
6 departure size (≈ 4.5 mm) and transport overpotential. More interestingly, it can be seen that only
7 these large bubbles periodically grew and departed from the WE, whereas most of the surrounding
8 small bubbles remained a residing state for $\Theta_{PTFE} = 0.55$ and 0.76 (see Figure S3 and Supplemental
9 Video S3 and S4 for bubble dynamics visualization). In addition, a few of the surrounding bubbles
10 could even shrink associated with the simultaneous growth of the neighboring large bubble (see
11 Supplemental Video S5 for bubble dynamics visualization). Figure 2K shows the time evolution
12 of the transport overpotential for the PTFE coverage of zero and 0.76 under 400 mA/cm^2 .
13 Compared with the condition of $\Theta_{PTFE} = 0$, the fluctuation of the transport overpotential for Θ_{PTFE}
14 $= 0.76$ showed higher amplitude but lower frequency. The frequency of transport overpotential for
15 $\Theta_{PTFE} = 0.76$ was consistent with the departure frequency of the large bubbles (see the inset of
16 Figure 2K and Supplemental Video S3), indicating the behavior of these large bubbles plays a
17 significant role in the transport overpotential.⁴⁸ To further understand the relationship between the
18 above bubble behaviors and the corresponding transport overpotentials, we characterized the
19 bubble dynamics by leveraging the wetting state analysis as follows of our study.



1

2 **Figure 2. Alkaline water splitting experiments with porous electrodes with various PTFE**

3 **coverage.**

4 (A) Schematic of the water splitting experiment setup. The overpotential at the working electrode

5 was recorded by a potentiostat. Bubbles were visualized by a high-speed camera from the side and

6 the DSLR from the top.

7 (B) Transport overpotential as a function of current density. The activation and ohmic

8 overpotentials have been subtracted from the measured overpotential. The error bars represent the

9 standard deviation due to the time-average of data points.

1 (C), (D), (E), (F) Side views of oxygen bubbles at 400 mA/cm^2 with PTFE coverage of 0, 0.16,
2 0.55 and 0.76, respectively. Scale bars are all 2 mm.

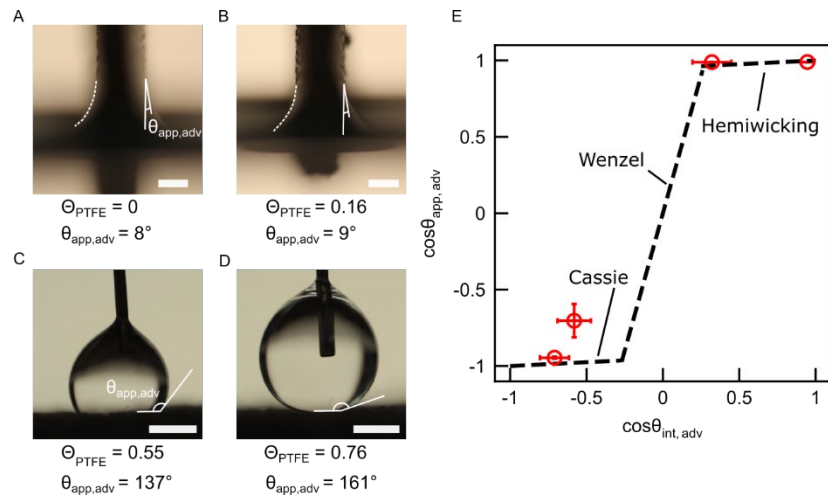
3 (G), (H), (I), (J) Top views of oxygen bubbles at 400 mA/cm^2 with PTFE coverage of 0, 0.16, 0.55
4 and 0.76, respectively. Scale bars are all 2 mm. The blurriness of images in G and H was due to
5 the interference of bubbles.

6 (K) Time transition of transport overpotentials at 400 mA/cm^2 with PTFE coverage of 0, 0.76.
7 Inset shows the images of repetitive bubble growth on the hydrophobic porous electrode in the
8 interval of 3.3 s which corresponds to the fluctuation of the transport overpotential.

9

10 Figure 3 shows the wettability analysis of WE with different PTFE coverage using 1 M KOH
11 solution. The WE was highly wicking when the PTFE coverage was zero and 0.16 as shown in
12 Figures 3A and 3B. The apparent contact angle was 8° and 9° for the PTFE coverage of zero and
13 0.16, respectively, which was determined by the Wilhelmy plate method.⁴⁹ However, the WE
14 became hydrophobic when the PTFE coverage increased to 0.55 and changed to superhydrophobic
15 (apparent contact angle $> 150^\circ$) when the PTFE coverage further increased to 0.76 as shown in
16 Figures 3C and 3D. We determined the droplet apparent contact angle on the non-wicking WE. A
17 partial Cassie state droplet⁵⁰ (137° apparent contact angle) was observed on the WE with the PTFE
18 coverage of 0.55, while a Cassie state droplet (161° apparent contact angle) was seen when the
19 PTFE coverage was 0.76. This significant transition in wetting state can be explained by a
20 combined effect of the porous structure and the PTFE deposition. To quantify this transition
21 behavior, we derived the modified Cassie-Baxter and Wenzel equations, which describe the
22 apparent contact angles of liquid on a composite interface of gas, liquid and solid material (See

1 Supplemental Information for details of wetting state equations). Figure 3E shows that the
 2 relationship between the apparent advancing contact angle $\theta_{app,adv}$ and internal contact angle $\theta_{int,adv}$
 3 in all of these four wetting states can be well-described by the modified Cassie-Baxter and Wenzel
 4 equations (dashed line in Figure 3E), using the experimentally determined solid fraction 0.02 and
 5 roughness factor 3.6 as the inputs (see Supplemental Information for details). Note the internal
 6 contact angle at the inner wall of the porous structure where the surface was chemically
 7 heterogenous and rough was determined by placing the droplet on a flat nickel substrate with the
 8 same PTFE coverage (see Supplemental Information for details).



9
 10 **Figure 3. Wettability characterization for wicking/non-wicking porous electrodes with**
 11 **various PTFE coverage. The working fluid is a 1 M KOH solution.**

12 (A), (B) Wilhelmy plate method for wicking electrodes. Apparent advancing contact angle $\theta_{app,adv}$
 13 of 8° , 9° , respectively with a PTFE coverage Θ_{PTFE} of 0 and 0.16, respectively. Dashed lines
 14 represent liquid-gas interfaces. Scale bars are 1 mm.

1 (C), (D) Sessile droplet contact angle measurement for non-wicking electrodes. Apparent
2 advancing contact angle $\theta_{app,adv}$ of 137° and 161° , respectively with a PTFE coverage Θ_{PTFE} of
3 0.55 and 0.76, respectively. Scale bars are 1 mm.

4 (E) Wetting states of 1 M KOH solution on porous electrodes. The internal advancing contact
5 angle $\theta_{int,adv}$ was estimated from the PTFE coverage. Dashed lines are theoretical predictions for
6 the hemiwicking, Wenzel and Cassie states. The error bars represent the uncertainty for the
7 apparent contact angle measurements and for the internal contact angle estimation.

8

9 We explained the significant change in bubble dynamics and transport overpotential considering
10 the wettability effect. In general, the bubble dynamics showed three distinct modes, *i.e.*, internal
11 growth and departure (Figure 4A), wicking (Figure 4B) and gas-filled modes (Figure 4C) due to
12 different bubble growth, departure and coverage mechanisms. Specifically, in the internal growth
13 and departure mode (Figure 4A), *i.e.*, the WE was not covered by PTFE, bubble nucleation and
14 departure occurred both on the surface and inside of the porous foam, because the bubble departure
15 diameter was smaller than the pore diameter ($\sim 200 \mu\text{m} - 700 \mu\text{m}$) in this highly wicking state.
16 The bubble departure diameter was $150 \pm 40 \mu\text{m}$ from a direct measurement of 100 bubbles. We
17 estimated the bubble growth using a combined experiment and modeling approach under the
18 diffuse-controlled growth condition, where an empirical parameter, *i.e.*, the gas efficiency f_g ,
19 which is the ratio of the number of molecules used for bubble generation to the total number of
20 molecules generated by the reaction, was incorporated (see Supplemental Information for details
21 about the bubble growth analysis).^{11,51,52} Figure 4D shows the bubble radius R as a function of
22 growth time t for the internal growth and departure mode under 400 mA/cm^2 with different gas

1 efficiencies. The values of f_g were determined from a typical range of gas efficiency which was
2 reported by literature.^{51,53} According to this bubble growth analysis, the growth coefficient b (*i.e.*,
3 $R = b\sqrt{t}$) for the internal growth and departure mode ranged from 0.12 mm/s^{0.5} to 0.20 mm/s^{0.5}.

4 When the WE was operated in the wicking mode, *i.e.*, the PTFE coverage increased to 0.16, the
5 bubble departure diameter became comparable to the pore diameter due to the slight decrease of
6 wettability. The bubble departure diameter was 450 ± 390 μm from a direct measurement of 100
7 bubbles. Although nucleation still occurred both on the surface and inside the WE, direct bubble
8 removal from the internal pores was significantly suppressed because of the increased bubble size
9 and frequent bubble coalescence (Figure 4B). Figure 4E shows the growth of a representative
10 bubble (marked by the red circle in the insets) in the wicking mode under 400 mA/cm². The
11 discontinuity of bubble radius at $t = 1.2$ s indicates the moment of bubble coalescence (see the
12 insets of Figure 4E at $t = 1.1$ s before coalescence and $t = 1.3$ s after the coalescence), which can
13 be commonly seen for the bubbles in the wicking mode (see Figure S5A and Supplemental
14 Information for details). Before coalescence, the evolution of bubble radius followed the diffuse-
15 controlled growth where the growth coefficient of this bubble was 0.26 mm/s^{0.5} in Figure 4E. We
16 characterized more bubbles as shown in Figure S5A. The growth coefficient for the wicking mode
17 ranged from 0.17 mm/s^{0.5} to 0.32 mm/s^{0.5}, which is comparable to the growth coefficient estimated
18 in the internal growth and departure mode.

19 When the PTFE coverage increased to 0.55 and 0.76, the WE transitioned to a gas-filled mode
20 (Figure 4C). The existence of this gas-filled mode can be confirmed by the following experimental
21 evidence. Specifically, according to the wetting state analysis (Figures 3E), the WE became
22 hydrophobic or superhydrophobic (Figure 3D) and Wenzel bubbles were observed, indicating a
23 strong resistance to liquid filling. Since only the large bubbles could periodically grow and depart

1 from the WE (see Figure S3 and Supplemental Video S3 and S4), we characterized the growth of
2 these large bubbles under 400 mA/cm^2 . Figure S5B shows that the growth coefficient of the large
3 bubbles ranged from $1.4 \text{ mm/s}^{0.5}$ to $1.6 \text{ mm/s}^{0.5}$ which is an order of magnitude larger than the
4 growth coefficients observed in the internal growth and departure and the wick modes under the
5 same current density (400 mA/cm^2). This high growth rate of the large bubbles indicates that there
6 is gas transport from the surrounding small bubbles to the large bubbles through the interconnected
7 pores in the WE, which is driven by the capillary pressure due to the larger curvature of smaller
8 bubbles as sketched in Figure 4C. Therefore, although the radius of large bubbles followed the
9 diffuse-controlled growth relationship, the detailed bubble growth mechanism needs to be further
10 investigated in future work due to the distinct gas transport process in the gas-filled mode. The
11 small bubbles would not grow or depart if the gas generation rate in these bubbles was equal to the
12 gas transport rate from the small bubbles to the large bubbles at a steady state (see Supplemental
13 Video S3 and S4). In addition, direct evidence for the gas-filled mode is the shrinking bubble
14 observed in a few of our experiments. Figure 4F shows the evolution of a shrinking bubble (marked
15 by 1 in the inset) and a neighboring growing bubble (marked by 2 in the inset), which can be also
16 seen in Supplemental Video S5. The bubble 1 slowly grew before 1.4 s followed by a sudden
17 shrinkage between 1.4 s and 1.9 s (insets of Figure 4F). Meanwhile, there was simultaneous growth
18 of bubble 2. Bubble 2 departed from the WE at 1.8 s whereas at the same moment, bubble 1 started
19 to grow again. This highly correlated shrinkage and growth shown in bubbles 1 and 2 indicates
20 that these two bubbles were connected through the gaseous pores in the WE.

21 Figure 4G shows that relationship between the bubble departure diameter and WE wettability can
22 be well-captured by the classical Fritz correlation,⁵⁴ which equates the bubble holding force at the
23 three-phase contact line with the bubble buoyancy ($D_b = 0.0208\theta_{app,rec}\{\gamma_{lv}/[g(\rho_l - \rho_v)]\}^{1/2}$)

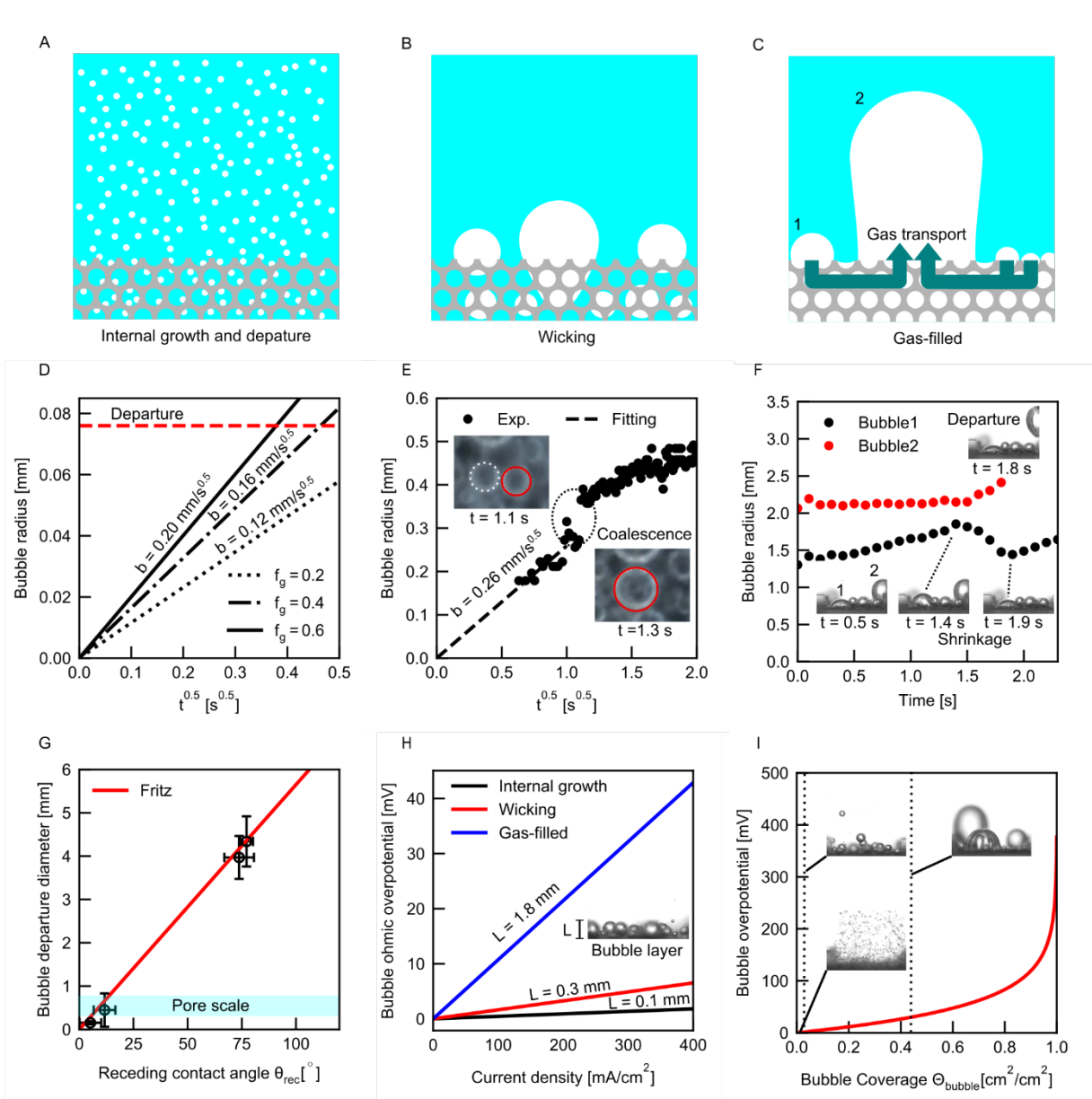
1 where D_b is the bubble departure diameter, $\theta_{app,rec}$ is the apparent receding contact angle (unit:
2 degree), γ_{lv} is the surface tension, g is the gravitational acceleration, and ρ_l, ρ_g are the density of
3 liquid and gas, respectively). Note that the internal receding contact angle was used for our analysis
4 when the bubble departure diameter was smaller or comparable to the nickel foam pore scale,
5 whereas the apparent receding contact angle was applied when the bubble departure diameter was
6 much larger than the pore scale. The bubble departure diameter for the PTFE coverage of 0.55 and
7 0.76 was determined from the average of 17 and 28 bubbles, respectively.

8 The significant change of bubble growth, departure diameter and wetting state from the internal
9 growth and departure mode to the gas-filled mode leads to the change of bubble coverage, bubble
10 layer thickness, and gas void fraction, which induces different transport overpotentials. Figure 4H
11 shows the bubble ohmic potential $\eta_{ohm,bub}$ as a function of current density for the internal growth
12 and departure ($\Theta_{PTFE} = 0$), wicking ($\Theta_{PTFE} = 0.16$), and gas-filled ($\Theta_{PTFE} = 0.76$) modes. The bubble
13 ohmic potential $\eta_{ohm,bub}$ was estimated using the experimentally determined bubble layer thickness
14 L and gas void fraction f_b (see Supplemental Information for details).^{28,29} The bubble layer
15 thickness was given by the time-average of bubble radius and bubble contact angle, and the void
16 fraction was determined from the time-average of bubble volume (see Supplemental Information
17 for details). Although the gas void fractions were similar for the internal growth and departure
18 mode ($f_b \approx 0.07$), wicking mode ($f_b \approx 0.08$), and gas-filled mode ($f_b \approx 0.08$), the bubble layer
19 thickness L (see the inset of Figure 4H) increased from about 0.1 mm to 1.8 mm due to the increase
20 of bubble departure diameter, leading to a significant increase of the bubble ohmic overpotential
21 for the gas-filled mode (Figure 4H). On the other hand, Figure 4I shows the bubble overpotential
22 η_{bub} as a function of bubble coverage Θ_{bubble} . In this work, we estimated bubble coverage by
23 analyzing the ratio of total bubble base area to the projected area (10 mm×10 mm) of the electrode

1 from the top view images and bubble contact angles, which were about 0.001, 0.015, and 0.47 for
2 the internal growth and departure mode ($\Theta_{PTFE} = 0$), wicking mode ($\Theta_{PTFE} = 0.16$), and gas-filled
3 mode ($\Theta_{PTFE} = 0.76$), respectively (see Figure S6 and Supplemental Information for details). The
4 increase of bubble coverage with PTFE coverage mainly resulted from the increase of bubble
5 contact angle. Note that the experimentally estimated bubble coverage for the projected area (10
6 mm×10 mm) is the lower limit of the actual bubble coverage for the entire porous structure, since
7 the bubble covered area inside the porous structure was not taken into account. For the internal
8 growth and departure mode, bubble nucleation and growth should homogeneously occur both
9 inside the porous structure and on the surface of the WE, because the bubble departure diameter is
10 smaller than the pore diameter. The experimentally estimated bubble coverage was thus close to
11 the actual bubble coverage in this mode. However, for the gas-filled mode, since the internal
12 porous structure of the WE was covered by gas, the actual bubble coverage can be larger than the
13 experimentally estimated bubble coverage. These experimentally estimated bubble coverages are
14 marked as the dashed lines in Figure 4I, where the induced bubble overpotential can be very small
15 for the internal growth and departure and wicking modes, while it can be comparable with the
16 bubble-induced ohmic overpotential for the gas-filled mode. Compared to the estimated bubble-
17 induced ohmic overpotential and bubble overpotential with the total transport overpotential, the
18 increase of transport overpotential from the internal growth and departure mode to the wicking
19 mode can be attributed to the increase of concentration overpotential. The concentration
20 overpotential could arise from the transport resistance inside the WE, where the species transport
21 inside the porous structure becomes inefficient due to the suppression of bubble removal. Direct
22 experimental characterizations of the concentration overpotential are desirable to further support
23 the above hypothesis, which is practically challenging due to the complex porous nature of the

1 WE. On the other hand, the increase of transport overpotential from the wicking mode to the gas-
 2 filled mode mainly resulted from the bubble-induced ohmic overpotential and bubble
 3 overpotential, *i.e.*, the transport resistance on the surface of the WE due to the increase of bubble
 4 departure diameter and contact angle.

5



6

1 **Figure 4. Bubble dynamics on porous electrodes with different wettability and its effect on**
2 **overpotential.**

3 (A) (B) (C) Schematics of bubble growth and departure modes. A, Hydrophilic electrode and the
4 bubble departure size smaller than the pore size. B, Hydrophilic electrode and the bubble departure
5 size comparable to or larger than the pore size. C, Hydrophobic electrode where the bubble
6 departure size was dictated by the macroscopic receding contact angle.

7 (D) (E) (F) Characterizations of the bubble growth in the internal growth and departure, wicking
8 and gas-filled modes. D, Bubble radius as a function of time under 400 mA/cm^2 current density in
9 the internal growth and departure mode. The bubble growth was estimated using an experiment
10 and modeling combined approach with the gas efficiency f_g as an empirical parameter (see
11 Supplemental Information for details). E, Bubble radius as a function of time under 400 mA/cm^2
12 current density in the wicking mode. The discontinuity of bubble radius at 1.2 s is attributed to the
13 bubble coalescence. Insets: top view image before the bubble coalescence ($t = 1.1 \text{ s}$) and after the
14 bubble coalescence ($t = 1.3 \text{ s}$), where the red circle indicates the bubble being measured and the
15 white dashed circle represent the neighboring bubble interacting with the red circled bubble. F.
16 Bubble radius as a function of time under 200 mA/cm^2 current density in the gas-filled mode. Two
17 neighboring bubbles were measured. Insets: time-lapse images of bubble evolution at $t = 0.5 \text{ s}$, t
18 $= 1.4 \text{ s}$, $t = 1.8 \text{ s}$ and $t = 1.9 \text{ s}$ where the shrinking bubble is marked as bubble 1 and the departed
19 bubble is marked as bubble 2.

20 (G) Bubble departure diameter as a function of the receding contact angle. The internal receding
21 contact angle and the macroscopic receding contact angle were used for wicking electrodes and
22 non-wicking electrodes, respectively. Solid line shows the Fritz equation. The light blue band

1 indicates the pore diameter ($\sim 200 \mu\text{m} - 700 \mu\text{m}$). The error bars are determined from the standard
2 deviations of multiple-time measurements.

3 (H) Bubble-induced ohmic overpotential as a function of current density for different bubble
4 growth and departure modes. Eq. S26 was used for the estimation of bubble-induced ohmic
5 overpotential. The bubble layer thickness and gas void fraction were determined from
6 experimental characterizations (see Supplemental Information for details). Inset: a side view image
7 of bubbles in the bubble layer.

8 (I) Bubble overpotential estimation as a function of the bubble coverage. The bubble coverage
9 drastically changes for various bubble departure modes (insets). Eq. S8 was used for the
10 estimation. The Tafel slope $RT/\{(1 - \alpha)F\} = 0.051$, where α is charge transfer coefficient, F is
11 Faraday constant, R is universal gas constant and T is temperature, respectively. The dashed lines
12 indicate the experimentally estimated bubble coverages for the internal growth and departure
13 mode, wicking mode, and gas-filled mode, respectively (see Supplemental Information for details).
14 Insets: side view images for the bubble morphologies in the internal growth and departure,
15 wicking, and gas-filled modes.

16
17 According to the insights gained from the wettability effect and bubble dynamics, we extracted an
18 important design parameter ζ for the porous electrode, *i.e.*, the ratio of the bubble departure
19 diameter to the pore diameter, which triggers the transition from an internal bubble growth and
20 departure mode (Figure 4A) to a wicking mode (Figure 4B). This design parameter indicates that
21 reducing the pore size at the same porosity is not always effective to improve the overall gas
22 production although more reaction area can be created. A better understanding of bubble de-

1 pinning mechanisms is also helpful to avoid the transition to the wicking mode.⁵⁵ To take full
2 advantage of the surface area enhancement using a porous structure in a mass transport loss
3 dominated regime, the pore size needs to be larger than the bubble departure size on the same
4 electrode to enable efficient bubble removal (*i.e.*, $\zeta < 1$), which can be realized by either
5 engineering the pore size without much change of the wettability or tuning the wettability for a
6 fixed pore size in practice. For this reason, a general design procedure can be proposed for the
7 mass transport loss dominated regime. Firstly, for a given wettability, which might be determined
8 from the optimal material kinetics of catalysts, the wetting state of the WE can be predicted by the
9 modified Cassie-Baxter and Wenzel equations. Then, the corresponding bubble departure diameter
10 D_b can be estimated by a correlation such as the Fritz equation with the wetting state as the input.
11 Next, the design parameter ζ can be calculated. If $\zeta > 1$, either the pore size or the wettability
12 should be increased. Finally, the above procedures should be iterated with the updated pore size
13 and wettability until $\zeta < 1$ is met.

14

15 In this work, we demonstrated a significant change in bubble dynamics and transport overpotential
16 during alkaline water splitting observed on the PTFE-deposited nickel foam electrode. We used
17 the nickel foam with various PTFE coverage to change the wetting characteristics from a highly
18 wicking state to superhydrophobic state, which were well-predicted by modified Cassie-Baxter
19 and Wenzel equations. The increase of WE hydrophobicity increased the bubble departure
20 diameter, bubble coverage and bubble layer thickness, and therefore increased the transport
21 overpotential. More importantly, we observed three types of bubble departure and growth modes
22 which are characterized by internal bubble growth and departure, wicking and gas-filled
23 electrodes. The water splitting performance on porous electrodes is very sensitive to the wettability

1 because the reaction area enhancement due to porous electrode diminishes when the bubble
2 departure size becomes comparable or larger than the pore size. This result indicates the ratio of
3 bubble departure diameter and pore diameter is an essential design parameter for high-efficiency
4 water splitting system. The proposed study elucidates the physical insights which relate the
5 wettability effect to the bubble dynamics and overpotential on a porous electrode. Furthermore,
6 when a given catalyst is identified for optimized kinetics at the laboratory scale, this work fills the
7 gaps about how to potentially design the architecture of the electrode based on the wettability of
8 the catalyst and/or substrate and can thus bridge the fundamental materials studies with
9 electrolyzer design.

10

11 **EXPERIMENTAL PROCEDURES**

12 **Sample preparation**

13 The nickel porous foam (bulk density 0.45 g/cm^3 , thickness 1.6 mm, porosity 95%, Goodfellow)
14 was used as the starting electrode material (Figure 1B). The nickel porous foam was sonicated in
15 5 M HCl solution for 20 min to remove oxide layer on the nickel surface (Figure S10). It was
16 subsequently rinsed in deionized (DI) water and ethanol and dried in air flow.

17 A typical Watt bath was used for the nickel electrodeposition to fabricate the hydrophilic surface.
18 The PTFE powder was added into the Watt bath for the nickel-PTFE co-deposition to obtain the
19 hydrophobic surface.⁴⁴ The compositions of chemicals dissolved in DI water are listed in Table
20 S1. The PTFE powder was added in DI water with cetyltrimethylammonium bromide (CTAB) for
21 dispersion. The PTFE dispersion was mixed by a stirrer at 800 rpm for 1 day and sonicated for 60

1 min. The platinum wire electrode and the Ag/AgCl electrode were used as a counter electrode and
2 a reference electrode, respectively. The nickel porous foam was fixed by an electrode holder and
3 immersed in the electrolyte. The electrolyte was agitated by the stirrer at 400 rpm during the
4 experiment. 1.2 V vs. Ag/AgCl of voltage was applied for 10 - 60 min at 60 °C.

5

6 **Sample characterization**

7 The surface structure of the porous electrodes was visualized by a scanning electron microscopy
8 (Zeiss Merlin High-resolution SEM, Zeiss) with 1.5 kV accelerating voltage. At least, 18 images
9 were taken at different positions for each sample. The average PTFE coverage was estimated from
10 the obtained images.

11

12 **Alkaline water splitting experiment**

13 All electrochemical experiments with nickel foam were performed on a pool gas-evolving
14 reaction rig shown in Figure 2A. The electrochemical measurements were carried out with a
15 potentiostat (VSP-300, BioLogic). The nickel foam was set on the fixture and connected to the
16 PTFE coated nickel wire (Figure S4). The graphite electrode and the Ag/AgCl electrode were used
17 as a counter electrode and a reference electrode, respectively. Nitrogen gas was induced into the 1
18 M KOH solution for 15 min to remove dissolved gases before starting experiment. During the
19 experiment, the space above the electrolyte in the bath was filled with nitrogen to prevent
20 dissolution of gasses into the electrolyte. The uncompensated resistance between the working
21 electrode and the reference electrode was measured by electrochemical impedance spectroscopy

1 (EIS; see Figure S2 in Supplemental Information for details). The overpotential between the
2 working electrode and the reference electrode for OER in 1 M KOH solution was measured by the
3 linear sweep voltammetry at scan rate 1 mV/s. Current step measurements at 50, 100, 200, 300,
4 400 mA/cm² were conducted for the bubble visualization and transport overpotential analysis.
5 Oxygen bubbles were visualized by the high-speed camera from the side of the vial. The frame
6 rate and the spatial resolution of the high-speed camera were 100 fps and about 11 μm/pixel
7 respectively. Moreover, the electrode surface was visualized by the DSLR from the top view. The
8 frame rate and the spatial resolution of the DSLR were 30 fps and about 17 μm/pixel respectively.

9

10 **Nickel foam wettability test and analysis**

11 Apparent advancing and receding contact angle on the nickel porous foam was characterized by
12 the Wilhelmy method for hydrophilic surfaces and sessile drop method for hydrophobic surfaces.
13 The shape of meniscus on the porous foam was measured with a DSLR (Canon, EOS rebel T3)
14 and a macro lens (MP-E 65mm f/2.8 x 1–5 Macro Photo, Canon). Contact angles were analyzed
15 by circle and ellipse best fittings with ImageJ. Several measurements, typically five times, were
16 conducted to specify the uncertainty of the measurements. The internal contact angle of nickel
17 foam was estimated from a correlation as a function of PTFE coverage. The correlation was
18 developed based on sessile droplet measurements with PTFE deposited nickel plates. The specific
19 area of nickel porous foam was estimated by capillary rise test to estimate the roughness factor
20 (see Supplemental Information for details).

21

22 **SUPPLEMENTAL INFORMATION**

1 Supplemental Information can be found at XX (URL will be added).

2

3 **ACKNOWLEDGMENT**

4 R.I. acknowledges the support from TOYOTA CENTRAL R&D LABS., INC. L.Z. acknowledges
5 the support from the Singapore-MIT Alliance for Research and Technology (SMART) LEES
6 Program. K.L.W. acknowledges support from the U.S.-Egypt Science and Technology Joint Fund.
7 S.G. acknowledges the support from National Natural Science Foundation of China (Grant No.
8 51706135 and 51521004) and Shanghai Pujiang Program (Grant No. 20PJ1406800). This work
9 was performed in part at MIT MRSEC (Materials Research Science and Engineering Centers)
10 sponsored by the National Science Foundation.

11

12 **AUTHOR CONTRIBUTIONS**

13 R.I. and L.Z. contributed equally to this work. R.I. and E.N.W. conceived the initial idea and
14 designed experiments. R.I. fabricated the samples and carried out material characterization. R.I.,
15 L.Z., K.L.W., S.G., and M.H. performed the experimental analysis. R.I. and L.Z. interpreted the
16 experimental results and performed theoretical analysis. R.I. and L.Z. co-wrote the manuscript
17 with the input from K.L.W., S.G., and M.H. E.N.W. and B.M.G. edited the manuscript and guided
18 the work.

19

20 **DECLARATION OF INTERESTS**

21 E.N.W. is a member of the advisory board of *Joule*.

1

2 REFERENCES

- 3 1. Angulo, A., van der Linde, P., Gardeniers, H., Modestino, M., and Fernández Rivas, D.
4 (2020). Influence of bubbles on the energy conversion efficiency of electrochemical
5 reactors. *Joule*, 1–25.
- 6 2. Zhao, X., Ren, H., and Luo, L. (2019). Gas Bubbles in Electrochemical Gas Evolution
7 Reactions. *Langmuir* 35, 5392–5408.
- 8 3. Xiang, C., Papadantonakis, K.M., and Lewis, N.S. (2016). Principles and implementations
9 of electrolysis systems for water splitting. *Mater. Horizons* 3, 169–173.
- 10 4. Yang, H., Zhao, T.S., and Ye, Q. (2005). In situ visualization study of CO₂ gas bubble
11 behavior in DMFC anode flow fields. *J. Power Sources* 139, 79–90.
- 12 5. Van Der Linde, P., Peñas-López, P., Moreno Soto, Á., Van Der Meer, D., Lohse, D.,
13 Gardeniers, H., and Fernández Rivas, D. (2018). Gas bubble evolution on microstructured
14 silicon substrates. *Energy Environ. Sci.* 11, 3452–3462.
- 15 6. Walter, M.G., Warren, E.L., McKone, J.R., Boettcher, S.W., Mi, Q., Santori, E.A., and
16 Lewis, N.S. (2010). Solar water splitting cells. *Chem. Rev.* 110, 6446–6473.
- 17 7. Haussener, S., Xiang, C., Spurgeon, J.M., Ardo, S., Lewis, N.S., and Weber, A.Z. (2012).
18 Modeling, simulation, and design criteria for photoelectrochemical water-splitting systems.
19 *Energy Environ. Sci.* 5, 9922–9935.
- 20 8. Moussallem, I., Jörissen, J., Kunz, U., Pinnow, S., and Turek, T. (2008). Chlor-alkali

- 1 electrolysis with oxygen depolarized cathodes: History, present status and future prospects.
2 *J. Appl. Electrochem.* *38*, 1177–1194.
- 3 9. Zeng, K., and Zhang, D. (2010). Recent progress in alkaline water electrolysis for hydrogen
4 production and applications. *Prog. Energy Combust. Sci.* *36*, 307–326.
- 5 10. Vogt, H. (2000). Bubble coverage of gas-evolving electrodes in a flowing electrolyte.
6 *Electrochim. Acta* *45*, 4449–4456.
- 7 11. Vogt, H., and Balzer, R.J. (2005). The bubble coverage of gas-evolving electrodes in
8 stagnant electrolytes. *Electrochim. Acta* *50*, 2073–2079.
- 9 12. Lee, J.K., and Bazylak, A. (2021). Bubbles: The Good, the Bad, and the Ugly. *Joule* *5*, 19–
10 21.
- 11 13. Lee, J.K., Lee, C., Fahy, K.F., Zhao, B., LaManna, J.M., Baltic, E., Jacobson, D.L., Hussey,
12 D.S., and Bazylak, A. (2020). Critical Current Density as a Performance Indicator for Gas-
13 Evolving Electrochemical Devices. *Cell Reports Phys. Sci.* *1*, 100147.
- 14 14. Dukovic, J., and Tobias, C.W. (1976). The influence of attached bubbles on potential drop
15 and current distribution at gas-evolving electrodes. *J. Electrochem. Soc.* *134*, 331–343.
- 16 15. Janssen, L.J.J., Sillen, C.W.M.P., Barendrecht, E., and van Stralen, S.J.D. (1984). Bubble
17 behaviour during oxygen and hydrogen evolution at transparent electrodes in KOH solution.
18 *Electrochim. Acta* *29*, 633–642.
- 19 16. Gabrielli, C., Huet, F., Keddam, M., Macias, A., and Sahar, A. (1989). Potential drops due
20 to an attached bubble on a gas-evolving electrode. *J. Appl. Electrochem.* *19*, 617–629.

- 1 17. Lee, C.H., Zhao, B., Lee, J.K., Fahy, K.F., Krause, K., and Bazylak, A. (2020). Bubble
2 Formation in the Electrolyte Triggers Voltage Instability in CO₂ Electrolyzers. *iScience* 23,
3 101094.
- 4 18. Lu, Z., Zhang, L., Iwata, R., Wang, E.N., and Grossman, J.C. (2020). Transport-Based
5 Modeling of Bubble Nucleation on Gas Evolving Electrodes. *Langmuir* 36, 15112–15118.
- 6 19. Zhang, L., Iwata, R., Zhao, L., Gong, S., Lu, Z., Xu, Z., Zhong, Y., Zhu, J., Cruz, S., Wilke,
7 K.L., et al. (2020). Nucleation Site Distribution Probed by Phase-Enhanced Environmental
8 Scanning Electron Microscopy. *Cell Reports Phys. Sci.* 1, 100262.
- 9 20. Brussieux, C., Viers, P., Roustan, H., and Rakib, M. (2011). Controlled electrochemical gas
10 bubble release from electrodes entirely and partially covered with hydrophobic materials.
11 *Electrochim. Acta* 56, 7194–7201.
- 12 21. Zou, X., Liu, Y., Li, G.D., Wu, Y., Liu, D.P., Li, W., Li, H.W., Wang, D., Zhang, Y., and
13 Zou, X. (2017). Ultrafast Formation of Amorphous Bimetallic Hydroxide Films on 3D
14 Conductive Sulfide Nanoarrays for Large-Current-Density Oxygen Evolution
15 Electrocatalysis. *Adv. Mater.* 29.
- 16 22. Fujimura, T., Hikima, W., Fukunaka, Y., and Homma, T. (2019). Analysis of the effect of
17 surface wettability on hydrogen evolution reaction in water electrolysis using micro-
18 patterned electrodes. *Electrochem. commun.* 101, 43–46.
- 19 23. Ahn, S.H., Choi, I., Park, H.Y., Hwang, S.J., Yoo, S.J., Cho, E., Kim, H.J., Henkensmeier,
20 D., Nam, S.W., Kim, S.K., et al. (2013). Effect of morphology of electrodeposited Ni
21 catalysts on the behavior of bubbles generated during the oxygen evolution reaction in

- 1 alkaline water electrolysis. *Chem. Commun.* *49*, 9323–9325.
- 2 24. Jones, S.F., Evans, G.M., and Galvin, K.P. (1999). Bubble nucleation from gas cavities - A
3 review. *Adv. Colloid Interface Sci.* *80*, 27–50.
- 4 25. Chen, J., and Guo, L. (2019). Size effect of one-dimensional nanostructures on bubble
5 nucleation in water splitting. *Appl. Phys. Lett.* *115*.
- 6 26. Sakuma, G., Fukunaka, Y., and Matsushima, H. (2014). Nucleation and growth of
7 electrolytic gas bubbles under microgravity. *Int. J. Hydrogen Energy* *39*, 7638–7645.
- 8 27. Buehl, W.M., and Westwater, J.W. (1966). Bubble growth by dissolution: Influence of
9 contact angle. *AIChE J.* *12*, 571–576.
- 10 28. Leistra, J.A., Sides, P.J., Soc, J.E., Leistra, J.A., and Sides, P.J. (1987). Voltage Components
11 at Gas Evolving Electrodes. *J. Electrochem. Soc.* *134*, 2442–2446.
- 12 29. Kempler, P.A., Coridan, R.H., Lewis, N.S., and Lewis, N.S. (2020). Effects of bubbles on
13 the electrochemical behavior of hydrogen-evolving Si microwire arrays oriented against
14 gravity. *Energy Environ. Sci.* *13*, 1808–1817.
- 15 30. Vogt, H. (1990). The Concentration Overpotential of Gas Evolving Electrodes as a Multiple
16 Problem of Mass Transfer. *J. Electrochem. Soc.* *137*, 1179–1184.
- 17 31. Vogt, H., and Stephan, K. (2015). Local microprocesses at gas-evolving electrodes and their
18 influence on mass transfer. *Electrochim. Acta* *155*, 348–356.
- 19 32. Vogt, H. (2013). On the various types of uncontrolled potential increase in electrochemical
20 reactors - The anode effect. *Electrochim. Acta* *87*, 611–618.

- 1 33. Vogt, H. (2017). The Quantities Affecting the Bubble Coverage of Gas-Evolving
2 Electrodes. *Electrochim. Acta* 235, 495–499.
- 3 34. Lu, X., and Zhao, C. (2015). Electrodeposition of hierarchically structured three-
4 dimensional nickel-iron electrodes for efficient oxygen evolution at high current densities.
5 *Nat. Commun.* 6, 1–7.
- 6 35. Liu, J., Wang, J., Zhang, B., Ruan, Y., Lv, L., Ji, X., Xu, K., Miao, L., and Jiang, J. (2017).
7 Hierarchical NiCo₂S₄@NiFe LDH Heterostructures Supported on Nickel Foam for
8 Enhanced Overall-Water-Splitting Activity. *ACS Appl. Mater. Interfaces* 9, 15364–15372.
- 9 36. Rao, Y., Wang, Y., Ning, H., Li, P., and Wu, M. (2016). Hydrotalcite-like Ni(OH)₂
10 Nanosheets in Situ Grown on Nickel Foam for Overall Water Splitting. *ACS Appl. Mater.*
11 *Interfaces* 8, 33601–33607.
- 12 37. Zhang, P., Li, L., Nordlund, D., Chen, H., Fan, L., Zhang, B., Sheng, X., Daniel, Q., and
13 Sun, L. (2018). Dendritic core-shell nickel-iron-copper metal/metal oxide electrode for
14 efficient electrocatalytic water oxidation. *Nat. Commun.* 9, 1–10.
- 15 38. Jian, J., Yuan, L., Qi, H., Sun, X., Zhang, L., Li, H., and Yuan, H. (2018). Sn–Ni₃S₂
16 ultrathin nanosheets as efficient bifunctional water- splitting catalysts with a large current
17 density and low overpotential.
- 18 39. You, B., Jiang, N., Sheng, M., Bhushan, M.W., and Sun, Y. (2016). Hierarchically porous
19 urchin-like Ni₂P superstructures supported on nickel foam as efficient bifunctional
20 electrocatalysts for overall water splitting. *ACS Catal.* 6, 714–721.

- 1 40. Chaudhari, N.K., Jin, H., Kim, B., and Lee, K. (2017). Nanostructured materials on 3D
2 nickel foam as electrocatalysts for water splitting. *Nanoscale* *9*, 12231–12247.
- 3 41. Kang, Z., Alia, S.M., Young, J.L., and Bender, G. (2020). Effects of various parameters of
4 different porous transport layers in proton exchange membrane water electrolysis.
5 *Electrochim. Acta* *354*, 136641.
- 6 42. Stoerzinger, K.A., Hong, W.T., Azimi, G., Giordano, L., Lee, Y.L., Crumlin, E.J.,
7 Biegalski, M.D., Bluhm, H., Varanasi, K.K., and Shao-Horn, Y. (2015). Reactivity of
8 Perovskites with Water: Role of Hydroxylation in Wetting and Implications for Oxygen
9 Electrocatalysis. *J. Phys. Chem. C* *119*, 18504–18512.
- 10 43. Wakerley, D., Lamaison, S., Ozanam, F., Menguy, N., Mercier, D., Marcus, P., Fontecave,
11 M., and Mougél, V. (2019). Bio-inspired hydrophobicity promotes CO₂ reduction on a Cu
12 surface. *Nat. Mater.* *18*, 1222–1227.
- 13 44. Iacovetta, D., Tam, J., and Erb, U. (2015). Synthesis, structure, and properties of
14 superhydrophobic nickel-PTFE nanocomposite coatings made by electrodeposition. *Surf.*
15 *Coatings Technol.* *279*, 134–141.
- 16 45. McCrory, C.C.L., Jung, S., Peters, J.C., and Jaramillo, T.F. (2013). Benchmarking
17 heterogeneous electrocatalysts for the oxygen evolution reaction. *J. Am. Chem. Soc.* *135*,
18 16977–16987.
- 19 46. Zou, X., and Zhang, Y. (2015). Noble metal-free hydrogen evolution catalysts for water
20 splitting. *Chem. Soc. Rev.* *44*, 5148–5180.

- 1 47. Wenzel, R.N. (1936). Resistance of solid surfaces to wetting by water. *Ind. Eng. Chem.* 28,
2 988–994.
- 3 48. Gabrielli, C., Huet, F., and Nogueira, R.P. (2005). Fluctuations of concentration
4 overpotential generated at gas-evolving electrodes. *Electrochim. Acta* 50, 3726–3736.
- 5 49. de Gennes, P.-G., Brochard-Wyart, F., and Quéré, D. (2004). Capillarity and wetting
6 phenomena.
- 7 50. Su, J., Charmchi, M., and Sun, H. (2016). A Study of Drop-Microstructured Surface
8 Interactions during Dropwise Condensation with Quartz Crystal Microbalance. *Sci. Rep.* 6,
9 1–11.
- 10 51. Vogt, H. (1984). The rate of gas evolution of electrodes-I. An estimate of the efficiency of
11 gas evolution from the supersaturation of electrolyte adjacent to a gas-evolving electrode.
12 *Electrochim. Acta* 29, 167–173.
- 13 52. Van Der Linde, P., Moreno Soto, Á., Peñas-López, P., Rodríguez-Rodríguez, J., Lohse, D.,
14 Gardeniers, H., Van Der Meer, D., and Fernández Rivas, D. (2017). Electrolysis-Driven and
15 Pressure-Controlled Diffusive Growth of Successive Bubbles on Microstructured Surfaces.
16 *Langmuir* 33, 12873–12886.
- 17 53. Chin Kwie Joe, J.M., Janssen, L.J.J., van Strelen, S.J.D., Verbunt, J.H.G., and Sluyter, W.M.
18 (1988). Bubble parameters and efficiency of gas bubble evolution for a chlorine-, a
19 hydrogen- and an oxygen-evolving wire electrode. *Electrochim. Acta* 33, 769–779.
- 20 54. Fritz, W. (1935). Maximum volume of vapor bubbles. *Phys Z.*

1 55. Lohse, D., and Zhang, X. (2015). Surface nanobubbles and nanodroplets. *Rev. Mod. Phys.*
2 87, 981–1035.

3